ChemComm

Unraveling Chemical Processes during Nanoparticle Synthesis with Liquid Phase Electron Microscopy and Correlative Techniques

Journal:	*ChemComm*
Manuscript ID	CC-FEA-08-2023-003723.R1
Article Type:	Feature Article

Unraveling Chemical Processes during Nanoparticle Synthesis with Liquid Phase Electron Microscopy and Correlative Techniques

Amy Chen,[1,†] Thilini U. Dissanayake,[2,†] Jiayue Sun,[3,†] Taylor J. Woehl[2,*]

[1]Department of Materials Science and Engineering, University of Maryland, College Park, College Park, MD 20742, USA

[2]Department of Chemical and Biomolecular Engineering, University of Maryland, College Park, College Park, MD 20742, USA

[3]Department of Chemistry and Biochemistry, University of Maryland, College Park, College Park, MD 20742, USA

*Corresponding author, email: tjwoehl@umd.edu, phone: 301-405-1074

†These authors contributed equally

Abstract

Liquid phase transmission electron microscopy (LPTEM) has enabled unprecedented direct real time imaging of physicochemical processes during solution phase synthesis of metallic nanoparticles. LPTEM primarily provides images of nanometer scale, and sometimes atomic scale, metal nanoparticle crystallization processes, but provides little chemical information about organic surface ligands, metal-ligand complexes and reaction intermediates, and redox reactions. Likewise, complex electron beam-solvent interactions during LPTEM make it challenging to pinpoint the chemical processes, some involving exotic highly reactive radicals, impacting nanoparticle formation. Pairing LPTEM with correlative solution synthesis, *ex situ* chemical analysis, and theoretical modeling represents a powerful approach to gain a holistic understanding of the chemical processes involved in nanoparticle synthesis. In this feature article, we review recent work by our lab and others that has focused on elucidating chemical processes during nanoparticle synthesis using LPTEM and correlative chemical characterization and modeling, including mass and optical spectrometry, fluorescence microscopy, solution chemistry, and reaction kinetic modeling. In particular, we show how these approaches enable investigating redox chemistry during LPTEM, polymeric and organic capping ligands, metal deposition mechanisms on plasmonic nanoparticles, metal clusters and complexes, and multimetallic nanoparticle formation. Future avenues of research are discussed, including moving beyond electron beam induced nanoparticle formation by using light and thermal stimuli during LPTEM. We discuss prospects for real time LPTEM imaging and online chemical analysis of reaction intermediates using microfluidic flow reactors.

1. Introduction

The complexity of the nanochemistry involved in colloidal metal nanoparticle synthesis continues to intrigue scientists and drives sustained research efforts to understand growth mechanisms with the ultimate goal of rational synthesis of complex, multicomponent nanoparticles. The nanochemistry underlying well-established syntheses, such as gold nanorods and nanoparticles,[1–3] remains elusive and under continued investigation. For instance, there remain gaps in understanding the mechanisms for symmetry breaking,[4] nanoparticle nucleation and growth,[4] molecular scale reaction intermediates,[5,6] and formation mechanisms of multimetallic nanoparticles.[7,8] There remains debate about the rate limiting step involved in initial nanoparticle seed formation with potential limiting factors including nucleation, reaction kinetics, or other mechanisms.[9,10] Polte *et al.* proposed that metal nanoparticles do not form by nucleation but instead by aggregation of metal atoms into clusters and subsequently into nanoparticles, which is supported by x-ray scattering experiments.[10] Recent work has demonstrated the importance of the molecular structure of the initial nanoparticle seeds in determining the final shape and size of the nanoparticles;[6,11,12] however, the intermediate species remain poorly characterized due to a lack of *in situ* characterization methods with sufficient spatiotemporal resolution. Despite limited understanding of single component nanoparticles, increasing demands for enhanced functional properties have pushed chemists to synthesize more complex multimetallic nanoparticles, such as metallic heterostructures and high entropy alloy nanoparticles (HEAs),[13–16] with little understanding of the formation mechanisms. Complex chemical processes during multimetallic nanoparticle synthesis, such as preferential reduction, intermetal electron exchange, metal-ligand binding, and formation of molecular cluster intermediates, have made establishing a mechanistic framework elusive. It is likely that a generalized mechanism is not possible due to the dependence

of mechanism on the particular metal species involved in the synthesis.[17] For these reasons, experiments probing the nanochemistry of single and multimetallic nanoparticle synthesis remain critical to uncover the important physicochemical processes and reaction intermediates and unlock rational colloidal nanoparticle synthesis.

Seminal work developing microelectromechanical systems (MEMS) based *in situ* transmission electron microscopy (TEM) sample cells[18–20] has enabled liquid phase transmission electron microscopy (LPTEM) to become a central technique for probing formation mechanisms of colloidal nanoparticles.[21–27] Overall, LPTEM uniquely enables directly imaging *physical processes* occurring during metal nanoparticle formation, including nucleation,[25,28] shape change,[4,27,29,30] phase separation,[31,32] aggregation,[33] and coalescence.[34–37] On the other hand, only a few LPTEM studies have revealed *chemical information* during nanoparticle formation, such as nanoparticle composition using energy dispersive x-ray scattering (EDS) and electron energy loss spectroscopy (EELS).[38,39] More detailed chemical information, such as metal-ligand complex coordination chemistry, organic ligand-metal binding,[40] oxidation state, and molecular structure of intermediates,[5] remains outside the realm of LPTEM. Conventional MEMS based LPTEM sample cells using silicon nitride membrane windows can directly visualize metallic nanoparticles larger than about 1 nm in size in 500 – 1000 nm thick liquid.[41] Specialized LPTEM sample cells that limit the liquid layer thickness or utilize thinner membranes can achieve atomic resolution, albeit with large electron doses.[42,43] Graphene liquid cell (GLC) based TEM imaging has visualized nanoparticle growth at atomic resolution *via* the monomer attachment mechanism as well as the formation of multimetallic sub-nanometer clusters during formation of alloyed nanoparticles.[22,33] Electron microscopy resolves atoms and nanoparticles based on their elastic scattering and diffraction properties, but does not provide significant chemical information. While

EELS and EDS can provide some of this information, molecular scale intermediates like metal-ligand complexes are highly susceptible to electron beam damage. Recent work has elucidated the 3D atomic structure of preformed nanoparticles in liquid,[44] but it remains a significant unmet challenge to perform these tomographic reconstructions dynamically and with chemical information. Coupling LPTEM observations with *ab initio* computations enables inferring the nanochemistry of nanoparticle formation.[45,46] However, the lack of direct measurements of the nanoparticle chemistry and molecular structure of intermediate species prohibits direct determination of the nanochemistry. For multimetallic nanoparticles, such as heterostructured metal nanoparticles and HEAs, kinetic control over their composition and spatial distribution of metal species requires understanding the structure and chemistry of the nanoparticles during intermediate growth stages.[8,14,47]

Besides the limitation of LPTEM in providing primarily spatial image data, the complex radiation chemistry generated by electron beam radiolysis of the solvent makes it challenging to establish the chemical reactions involved in nanoparticle formation.[48,49] Electron beam induced growth remains the predominant method for stimulating nanoparticle formation during LPTEM, which has significant differences from standard solution chemical synthesis approaches.[50] Radiolysis simulations have become an essential tool for understanding redox chemistry during LPTEM imaging of nanoparticle formation and have enabled systematically varying reaction conditions by changing electron beam conditions.[26,51–55] While useful, radiolysis kinetic models are limited by the availability of kinetic data for each chemical species and its reaction products.

This feature article highlights recent work in our group and others focusing on concurrent use of LPTEM, correlative chemical analysis, wet chemistry, and radiolysis simulations to establish chemical processes mediating metal nanoparticle formation (**Fig. 1**). First, we describe the

radiolysis modified chemical environment during LPTEM and review recent work exploring radical reactions with metal ions, small organic molecules, and polymers typically used as organic capping ligands during nanoparticle synthesis. We review recent advances in detecting radiolysis products and simulating radiolysis during LPTEM. Next, we describe recent work that utilizes fundamental understanding of radiolysis reactions to establish LPTEM imaging conditions that produce redox environments similar to solution chemical synthesis of metal nanoparticles. The next section describes applications of LPTEM to investigate formation mechanisms and chemical processes occurring during synthesis of multimetallic nanoparticles. Specific studies discussed include using LPTEM to establish formation mechanisms of bimetallic alloys, HEA nanoparticles, and photodeposition of silver onto plasmonic gold nanorods. We conclude the article by offering perspectives on outstanding challenges for using LPTEM to probe nanoparticle formation in solution and future research avenues to address these challenges.

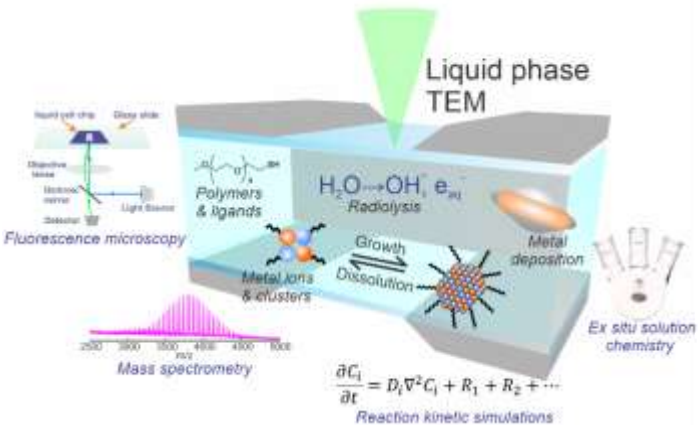

Fig. 1. LPTEM with correlative *ex situ* methods enables unveiling chemical processes during nanoparticle synthesis.

2. Radical driven redox chemistry and electron beam damage to organic molecules. In this section, we discuss recent work that has established how electron beam-solvent interactions impact redox chemistry, organic molecules and polymers used as capping ligands, and nanoparticle stability during LPTEM observation of nanoparticle formation. First, we briefly describe the aqueous phase radiation chemistry that is commonly utilized to stimulate nanoparticle formation and highlight recent work that established chemical conditions during LPTEM nanoparticle synthesis that are equivalent to wet chemistry. We then discuss recent advances that used redox couples and nanoparticle dissolution to probe the redox chemistry of aqueous solutions during LPTEM. Nanoparticle synthesis is strongly influenced by the concentration and functional groups on organic capping ligands, so we conclude this section by discussing radiation damage of organic matter and methods to mitigate the damage.

2.1. Overview of radiolysis and radical redox chemistry during LPTEM

The primary stimulus for nanoparticle growth and initiating other nanoscale processes during LPTEM imaging, such as self-assembly and polymerization, remains the imaging electron beam. While this method is not ideal due to the exotic and aggressive radicals that drive chemical reactions,[48] interactions between the electron beam and solvent are generally unavoidable save a few methods discussed below (*e.g.*, radiation resistant solvents, radical scavengers). Here we provide a brief overview of the radiation chemistry during LPTEM as a preface to reviewing recent works on nanoparticle synthesis and refer readers to prior works for more extensive descriptions of radiation chemistry during LPTEM.[26,48–51,53–55] Most of this article will describe experiments in aqueous solution, so we focus here on the radiation chemistry of water. Readers are referred to

recent work by the Gianneschi lab for radiolysis models of non-aqueous systems relevant to LPTEM.[56]

The electron beam dose rate during LPTEM, an average measure of the energy deposited per unit mass of material in units of Grays/s (Gy/s), is on the same order of magnitude as conventional high energy pulsed linear electron accelerators with microsecond pulse widths, each of which contain several Grays of dose. However, the electron flux and total electron dose delivered to the sample is orders of magnitude greater than in pulse radiation experiments due to the nanometer to angstrom sized electron beam and continuous irradiation of the sample during imaging. Radiolysis of neat water forms several oxidizing and reducing species: $H_2O \rightarrow H^+, OH^{\cdot}, e_{aq}^-, H^{\cdot}, OH^-, H_2O_2, H_2, HO_2^{\cdot}$.[55] Of primary importance are the oxidizing hydroxyl radical ($OH^{\cdot}$), which can oxidize metal species and generate radical sites on polymers and organic molecules,[57] and the aqueous electron (e_{aq}^-) and hydrogen radical ($H^{\cdot}$), which can reduce some metal ions and organic functional groups. The latter reducing radicals are widely believed to drive metal nanoparticle formation, while the former oxidizing radicals are thought to drive nanoparticle etching and oxidative damage to organic molecules. Oxidative radicals can etch nanoparticles or slow nanoparticle growth kinetics by oxidizing precursors. Alcohol solvents or use of hydroxyl radical scavengers can significantly mitigate unwanted oxidation during radiolytic synthesis of metal nanoparticles.[48] Aqueous electrons are significantly more reducing than typical reducing agents using in wet chemical synthesis,[58] but are produced at concentrations orders of magnitude lower than in wet chemical synthesis. Likewise, radiation chemical synthesis during LPTEM continuously injects reducing agents and metal precursor into the image area leading to continuous growth of nanoparticles. Wet chemical synthesis is a batch reaction where all reagents are depleted after the reaction, indicating the reaction kinetics and rate laws differ from LPTEM.[50]

2.2. Establishing electron beam induced synthesis conditions similar to solution chemistry

It remains challenging to translate LPTEM insights into nanoparticle formation mechanisms that are relevant to wet chemical synthesis due to the complex chemical environment produced by electron radiolysis of the solvent. Given the unavoidable nature of radiolysis during LPTEM, it is critical to establish experimental conditions that produce a redox environment that is relevant to wet chemical synthesis of nanoparticles. Recent work by Wang *et al.* rigorously compared synthesis of < 5 nm AuCu alloyed nanoparticles with electron irradiation during LPTEM and with sodium borohydride reduction to empirically establish LPTEM conditions that produce nanoparticles similar to those formed *ex situ*.[59] Here gold chloride and copper nitrate were co-reduced by electron beam radiolysis during LPTEM in the presence of thiolated polyethylene glycol (PEH-SH) capping ligands. Aqueous electrons and hydrogen radicals are the primary reducing species leading to the precipitation of metal nanoparticles, while oxidizing radicals can oxidatively etch the nanoparticles under certain conditions. In addition to oxidation of metal, the oxidizing radicals can damage organic molecules *via* hydrogen abstraction reactions, among other reactions. Prior work showed that complexation of the gold and copper ions with the PEG-SH formed multimetallic thiolate complex ions that facilitated alloying, while two-phase synthesis with no metal thiolate precursors formed gold nanoparticles with nearly no copper alloying.[60] Based on this prior observation, the study by Wang *et al.* utilized alloying extent in the AuCu nanoparticles as a proxy for radiation damage to the metal thiolate precursors and to establish experimental conditions during LPTEM that were similar to solution chemistry (**Fig. 2a**). In essence, production of nanoparticles under a certain set of LPTEM experimental conditions (precursor and ligand concentration, beam current, magnification, dose rate) with similar composition and size to wet chemical synthesis indicated the redox environment and reaction

conditions were similar. A similar empirical method was used by Liu and Mirsaidov *et al.*, where formation of cubic ZIF-8 metal organic framework (MOF) nanoparticles during LPTEM indicated synthesis conditions were similar to wet chemical synthesis and that MOFs were not significantly damaged by the electron beam.[31] Solution phase synthesis using aqueous sodium borohydride as a reducing agent formed 2 – 3 nm AuCu alloyed nanoparticles containing between 55 – 75 atomic% gold. Dose controlled continuous LPTEM imaging of the precursor solution showed that at relatively low electron dose rates < 20 MGy/s individual nanoparticles with sizes ranging from 1 – 8 nm formed (**Fig. 2b**). The particle size was overall larger than for sodium borohydride reduction, but the shape of the particle size distribution (PSD) was nearly the same, suggesting a similar growth mechanism.[61] At larger dose rates > 20 MGy/s particle aggregation dominated and formed irregular branched nanostructures that were almost entirely gold (**Fig. 2c**). Prior work has shown that large dose rates form more oxidizing radiolysis conditions,[55] which could oxidize metal thiolate precursors or copper metal atoms. The nanoparticles formed under low dose conditions had statistically indistinguishable composition and aggregation extent compared to those formed by sodium borohydride reduction (**Fig. 2d,e**). Critically, this work established LPTEM imaging conditions (dose rate, beam current, magnification) that formed nanoparticle that were chemically and physically similar to those synthesized by sodium borohydride reduction. The Gianneschi group found that silver containing MOFs formed during LPTEM with similar morphologies as wet chemical synthesis over a similar dose rate range as the AuCu nanoparticles,[62] which suggests a common damage mechanism at play.

Work by other groups has indicated that radiolysis-based synthesis during LPTEM can yield metal nanoparticles with similar physical and chemical characteristics compared to wet chemistry. Several prior works by the Alloyeau lab have demonstrated shaped controlled formation

of metal nanoparticles mediated by capping ligands, including nanostars and nanorods, using LPTEM.[30,63] While electron beam generated radicals led to faster nanoparticle growth kinetics compared to wet synthesis, the nanoparticle morphologies were similar to colloidal phase nanoparticles produced using a weak reducing agent. The authors concluded that while the kinetics differed quantitatively due to the aggressive reducing nature of solvated electrons, the overall growth mechanism for shape-controlled nanoparticle formation was preserved during LPTEM. Similarly, Tan *et al*. used LPTEM and radiolysis induced metal deposition to observe temperature mediated shell growth dynamics during palladium shell deposition on gold nanorods.[64] Near room temperature they observed kinetically dominated isotropic shell deposition, while at 80 °C they observed formation of thermodynamically preferred cubic shell morphologies, consistent with prior wet chemical synthesis.[65] Overall, these prior works demonstrate that LPTEM is capable of producing a redox environment that generates nanoparticles with similar attributes as wet chemical synthesis. This is an important step toward translating LPTEM experimental results to improve upon and discover new solution chemical synthesis methods for nanoparticles.

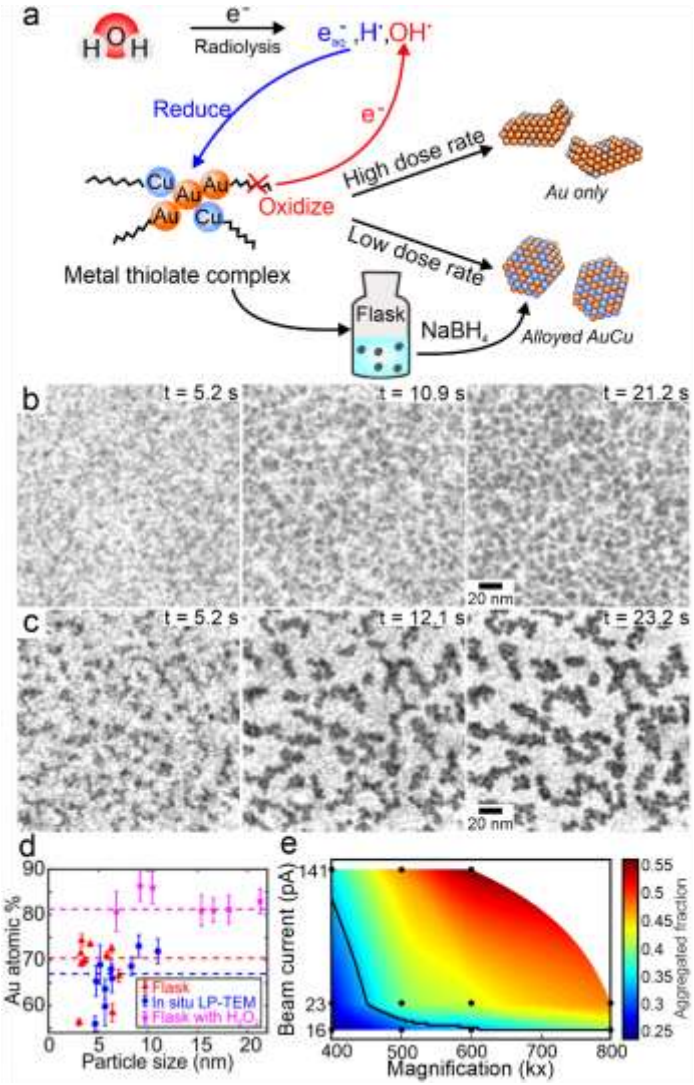

Fig. 2. Establishing LPTEM imaging conditions comparable to solution chemistry synthesis. (a) Schematic illustration of dose-controlled LPTEM synthesis of alloyed and phase separated AuCu nanoparticles from a multimetallic thiolate precursor. (b)-(c) Bright field scanning TEM (BF-STEM) images of nanoparticles growing under electron irradiation at dose rates of 17 MGy/s (b) and 65 MGy/s (c). (d) EDS derived composition of single AuCu nanoparticles prepared by several methods as a function of particle size. Dashed lines represent median nanoparticle compositions. (e) Aggregated fraction of AuCu nanoparticles as a function of LPTEM beam current and magnification compared to a sample prepared by sodium borohydride reduction (black solid line).

Adapted with permission from *ACS Nano*, 2021, **15**, 2578-2588. Copyright 2021 American Chemical Society.

2.3. Probing the redox environment during LPTEM with nanoparticle dissolution and redox couples

The reduction potential is a critical parameter for nanoparticle synthesis as it determines the reduction rate of metal ions,[58] which impacts nanoparticle size, shape, and alloying extent.[66,67] While the reduction potential can be manipulated during solution chemistry *via* choice of chemical reductant, temperature, and pH,[58] LPTEM researchers have far less control over this important parameter. Recent LPTEM experiments by the Alivisatos group have utilized nanoparticle/chemical etchant mixtures and metal ion redox couples to investigate redox chemistry during radiolysis. Hauwiller *et al.* exposed gold nanorods and nanocubes in GLCs to a chemical etchant, iron chloride, and electron beam irradiation and quantified the nanoparticle etching kinetics.[68] They showed that increasing the dose rate increased the etching rate while iron chloride concentration had no effect on the etching kinetics. This result suggested that electron beam generated radicals, primarily hydroxyl radicals, actively oxidized gold atoms on the nanoparticle surface. On the other hand, iron chloride produces a weak oxidizing agent, Fe^{2+}, which controls the reduction potential of the solution and therefore the types of surface atoms and facets that are being etched.[69,70] Higher concentrations of iron chloride enabled etching gold surface atoms with high coordination number. This work was extended using other redox couples to precisely control the electrochemical potential during LPTEM, enabling selective etching of multimetallic nanostructures.[71] Recent work by Crook *et al.* was the first to utilize EELS to investigate oxidation of Ce^{3+} ions by hydroxyl radicals in GLCs in the TEM.[72] Time resolved EELS measurements and

kinetic modeling of the Ce^{3+} oxidation rate showed that literature rate values were an order of magnitude lower than experiments. The authors posited the discrepancy was due to the close proximity of water molecules to cerium ions in the highly concentrated salt solution. Further, rate constants in the radiation chemistry literature are typically measured using microsecond pulsed radiation and ~MeV electron energies, in contrast to continuous radiation using 200 keV electrons during EELS measurements. Fitting of the oxidation reaction kinetics showed that the hydrogen gas G-value was nearly an order of magnitude larger than the literature value of 0.17 molecules H_2/100 eV. Recent work by Wang *et al.* found a similar G-value was required to describe the electron beam induced evaporation dynamics of water droplets during LPTEM imaging.[73] One explanation for the enhanced G-value of hydrogen gas in these two studies is that water radiolysis under continuous high dose rate electron irradiation is more similar to high linear energy transfer (LET) radiation, such as alpha particles, which produces closely spaced radiolysis spurs that enhance radical recombination into molecular species.[73] Prior works by Wang *et al.* and Grogan *et al.* estimated significant spur overlap during STEM imaging of liquids at moderate magnifications (~100,000 x), which supports this explanation.[74,75] Recent results from Mølhave lab directly quantified radical production in aqueous solution using electrochemistry and found evidence of hydrogen and sulfate radical production, but not hydrogen peroxide production.[76] The absence of hydrogen peroxide is in direct contrast to expectations from radiolysis models; however, the hydrogen peroxide concentration could be below the detection limit of the electrochemical measurement. Taken together, these results provide initial experimental evidence suggesting that LPTEM researchers should use literature G-values and rate constants derived from low dose rate experiments with caution and consider performing experimental data fitting or direct measurements to evaluate radiolysis kinetic parameters. Taken together, these observations

indicate new G-value measurements under conditions relevant to LPTEM, including high dose rate and total dose and nanoscale electron beam size, are needed to truly quantify the impact of the electron beam on solution chemistry.

2.4. Polymer-radical reactions during LPTEM

Discovery of LPTEM experimental conditions that closely mimic *ex situ* solution phase synthesis must also consider reactions between radicals and organic capping ligands. The molecular structure of organic molecules, specifically the anchoring and pendant functional groups, is critical to their function as capping ligands.[77] For instance, thiol terminated alkanes and oligo ethylene glycols are common capping ligands, where the thiol strongly binds to the metal nanoparticle surface.[12,78] Binding of capping ligands to metal precursors has been shown to impact the metal reduction rate, reaction intermediate concentrations, and nucleation and growth rates.[79,80] Changes to the pendant or anchoring function groups of capping ligands can have unwanted consequences on nanoparticle formation during LPTEM and lead to products that differ from wet chemical synthesis. Moreover, radiation damage to soluble organic molecules cannot typically be observed by LPTEM imaging, further emphasizing the need to understand and consider potential radical-ligand reactions.

There is a long history of polymer radiation chemistry, including the use of ionizing radiation in industrial production of polymers,[57,81,82] which provides a strong fundamental basis to interpret radical-polymer reactions during LPTEM.[83] Recent work by Wang *et al.* utilized radiolysis simulations to establish the impact of radicals on the structure of polyethylene glycol thiol (PEG-SH) capping ligands for nanoparticle synthesis (**Fig. 3a**).[59] The predominant reaction

between hydroxyl radicals and aqueous phase carbon-based polymers and alkanes is hydrogen abstraction from the carbon backbone to form alkyl macroradicals.[49] The alkyl radical subsequently forms intramolecular or intermolecular crosslinks with backbone or functional group carbons, which initiates a radical chain polymerization reaction. Intramolecular crosslinking is preferred when the polymer molecular weight and dose rate are relatively large, favoring formation of multiple radicals per polymer molecule.[82] On the other hand, intermolecular crosslinking is preferred for low polymer molecular weight and dose rate. Chain scission occurs when the alkyl radicals are long lived due to low dose rate or steric inhibition to crosslinking. Each of these reactions has been directly observed while imaging individual solution phase polymer molecules with GLC TEM.[84] In addition to polymer reactions, radicals interact with redox active functional groups on polymers, such as thiol anchoring groups on nanoparticle capping ligands. The standard reduction potential of a free thiol group ranges from 300 – 400 mV,[85] indicating it is readily oxidized by hydroxyl radicals and hydrogen peroxide to form disulfide bonds, which are in turn readily reduced by aqueous electrons and hydrogen radicals. The steady state concentrations of thiols and disulfides, together with intermediate radical species such as the thiyl radical ($R-S^{\cdot}$), are coupled with the radical concentrations and respective reaction kinetics. A numerical reaction-diffusion model developed by Wang *et al.* utilized rate constants for radical reactions with small molecule thiols and PEG to estimate the concentration of various PEG-SH-radical reaction products during electron beam induced synthesis of AuCu nanoparticles (**Fig. 3b**).[59] The model showed that the steady state PEG-SH concentration was < 10% of the initial concentration at a dose rate of ~1 MGy/s, corresponding to low magnification STEM imaging (~10,000 x). The PEG-SH concentration reduced to about 0.5% for the ~10 MGy/s condition used for LPTEM imaging (100,000 – 500,000 x magnification). The reaction products with the highest yields were hydroxyl

radicals, PEG macroradicals with the thiol group cleaved ($PEG^{\cdot}$), and thiyl radical functionalized PEG ($PEG-S^{\cdot}$). The nanoparticles likely remained stable under low dose LPTEM imaging because the thiyl radical strongly binds metal nanoparticle surfaces.[78] The hydroxyl radical concentration exceeded the initial PEG-SH concentration at dose rates > 20 MGy/s, which corresponded to experimental conditions where nanoparticle aggregation was observed. Potential mechanisms by which hydroxyl radicals caused nanoparticle aggregation by mechanisms include oxidative ligand detachment and intermolecular crosslinking of PEG-SH ligands between neighboring nanoparticles.[49,86]

The presence of interfaces and dispersed particles in the solvent has a significant impact on the radiolysis process. Modeling work by Gupta *et al.* showed that radical concentrations can be several times larger near a solid-liquid interface due to enhanced production of secondary electrons in the high atomic number solid.[87] Likewise, Korpanthy *et al.* recently demonstrated how gold nanoparticles enhance electron beam damage of aqueous phase PEG (**Fig. 3c**).[88] Here electron beam damage of aqueous PEG solutions during LPTEM deposited extended branched structures on gold nanoparticle surfaces. Correlative matrix assisted laser desorption ionization imaging mass spectrometry (MALDI-TOF IMS) showed that LPTEM imaging of aqueous PEG in the presence of gold nanoparticles degraded the polymer (**Fig. 3d**). Numerical reaction kinetic simulations accounting for enhanced electron scattering by the gold nanoparticles showed the total amount of PEG macroradicals formed increased as a function of gold nanoparticle concentration (**Fig. 3e**). Addition of isopropanol counteracted the sensitizing effect of the gold nanoparticles on electron damage by scavenging hydroxyl radicals (**Fig. 3e**).

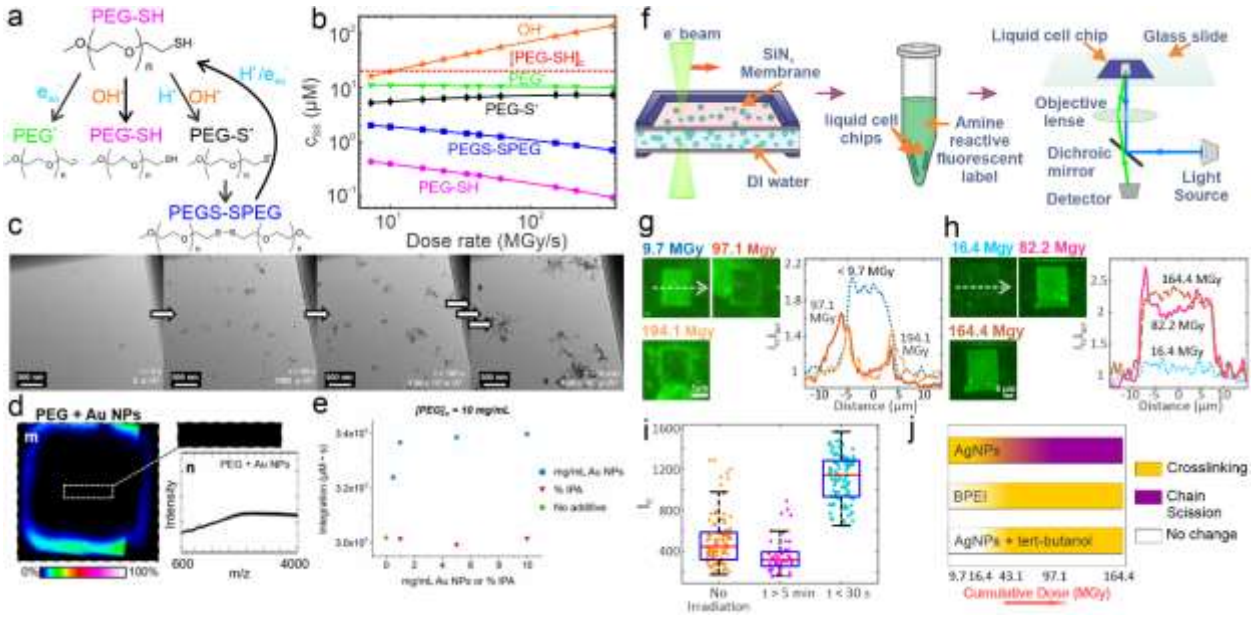

Fig. 3. Kinetic simulations and correlative characterization of polymer-radical reactions during LPTEM imaging. (a) Aqueous phase radiolysis reactions with PEG-SH capping ligands. (b) Steady state concentration of PEG-SH radiolysis reaction products as a function of electron beam dose rate. (a)-(b) Adapted with permission from *ACS Nano*, 2021, **15**, 2578-2588. Copyright 2021 American Chemical Society. (c) Electron beam induced damage to PEG in the presence of 100 nm gold nanoparticles. (d) MALDI-TOF IMS of the sample in (c) after LPTEM showing degradation of the PEG. (e) Radiolysis simulation of the amount of damaged PEG ($PEG^{\cdot}$) after 1000 seconds of LPTEM imaging in the presence of various additives. The dose rate was $7.5 \times 10^7 \frac{Gy}{s}$. (c)-(e) adapted with permission from *Nano Lett.*, 2021, **21**, 1141-1149. Copyright 2021 American Chemical Society. (f) Schematic illustration of LPTEM and correlative FM for probing radical reactions with polymer capping ligands. (g)-(h) FM images of LPTEM image areas containing silver nanoparticles and BPEI (g) and BPEI only (h) after irradiation with various total doses. The plots show cross-sections of the fluorescence intensity across the irradiated image area (white dashed arrows in (g) and (h)). (i) Fluorescence intensity of individual nanoparticles exposed to

various total doses. (j) Summary of the impact of LPTEM imaging on ligand-radical reactions as a function of solution conditions and total dose. (f)-(j) adapted with permission from *ACS App. Mat. Int.*, 2021, **13**, 37553-37562. Copyright 2021 American Chemical Society.

2.5. Electron beam damage to nanoparticle capping ligands during LPTEM

A recent study by Dissanayake *et al.* utilized correlative LPTEM and fluorescence microscopy (FM) to demonstrate that polymer-radical reactions chemically modified the silicon nitride membrane and nanoparticle surfaces.[89] Positively charged branched polyethyleneimine (BPEI) coated silver nanoparticles were deposited onto the silicon nitride membrane and imaged in water with LPTEM (**Fig. 3f**). The nanoparticles were imaged with STEM under different dose rates and total doses, modified by changing magnification, beam current, and time. After the experiment, the sample was disassembled and the amine moieties on the BPEI were labeled with an amine selective fluorescence probe and imaged with FM. Control experiments established the local fluorescence intensity in the FM images was proportional to the local BPEI concentration. Silver nanoparticles in DI water showed relatively bright fluorescence across the entire square image region when irradiated for < 30 s (< 9.7 MGy), indicating an increase in local BPEI concentration (**Fig. 3g**). This indicated that when the total electron dose was relatively low, intermolecular crosslinking reactions between free ligands dispersed in solution and ligands adsorbed on the membrane surface dominated to increase local BPEI coverage.[82] This behavior reversed at high cumulative doses (> 97.1 MGy) and irradiation times (> 5 min), where fluorescence intensity was lower or similar to pristine areas of the silicon nitride, indicating reduced BPEI coverage. This was likely due to a combination of increasing BPEI molecular weight, electrostatic repulsion between amine groups, and the decreasing local free ligand

concentration in solution. Together these factors shifted the system toward net chain scission reactions.[90,91] The ring of bright fluorescence intensity surrounding the irradiated areas at high dose rate suggested that the fragmented BPEI ligands solubilized in water and were transported out of the irradiated area by diffusion and/or beam induced electric fields. These measurements demonstrated an unexpected non-monotonic change in surface ligand coverage on nanoparticles as a function of dose rate. Counter to common assertions, these measurements suggest that low dose imaging cannot avoid radiation damage to organic molecules during LPTEM. In the absence of silver nanoparticles, LPTEM imaging of free BPEI ligands in solution resulted in predominantly intermolecular crosslinking reactions and buildup of BPEI over irradiation times up to 10 min (164.4 MGy) (**Fig. 3h**). The significantly brighter fluorescence intensity in the image area with nanoparticles compared to the case with no nanoparticles points towards acceleration of polymer-radical reactions by silver nanoparticles. As discussed above, this finding is in agreement with a previous study where damage to soluble polymers was amplified by gold nanoparticles (**Fig. 3c**).[88]

Fig. 3i shows that the fluorescence intensity of individual nanoparticles, *i.e.*, the BPEI ligand coverage, was highest for regions irradiated for < 30 s, followed by unirradiated regions, and finally by regions irradiated for > 5 min. This measurement again demonstrated that low total doses increased the BPEI ligand coverage compared to unirradiated regions due to net crosslinking reactions, while high total doses decreased the BPEI ligand coverage due to net chain scission. Addition of a hydroxyl radical scavenger, tert-butanol, was found to diminish electron beam modification to the BPEI surface ligand coverage. With tert-butanol added the authors observed a slower increase in BPEI concentration with increasing total dose compared to no scavenger conditions, indicating a decrease in the BPEI crosslinking rate. Decreasing BPEI coverage was not observed at any total dose tested, indicating the absence of chain scission in the presence of the

radical scavenger. **Fig. 3j** summarizes the impact of LPTEM on BPEI ligands under various conditions tested. Taken together, these results indicate a nuanced impact of the electron beam on nanoparticles surface ligands during LPTEM. While prior work assumed that electron irradiation monotonically degrades organic molecules with increasing total dose, this work demonstrated an increase in ligand coverage at low total doses followed by a decrease at high doses. In the context of nanoparticle synthesis, this work indicates that electron irradiation can non-monotonically modify the local concentration and molecular weight of capping ligands, which could impact the final nanoparticle size, shape, and growth kinetics. Likewise, this work emphasizes that electron beam damage to organic molecules does not involve a singular chemical mechanism but instead displays multiple damage modes that dominate over different total dose ranges.

3. LPTEM investigation of chemical processes during nanoparticle growth

3.1. Ligand mediated alloying in bimetallic nanoparticles

Deep understanding of the electron beam induced redox chemistry during LPTEM imaging together with correlative chemical analysis has enabled novel insights into the chemical processes occurring during synthesis of multimetallic nanoparticles. As shown in **Fig. 2**, Wang *et al.* demonstrated that alloyed AuCu nanoparticles formed under low dose LPTEM imaging, while aggregated Au nanoparticles formed under high dose rate imaging.[59] Nanoparticles synthesized from a mixture of multimetallic metal thiolates, which contained four metal sites occupied by either gold or copper atoms (**Fig. 4a**), formed alloyed AuCu nanoparticles and sub-nanometer metal clusters (**Fig. 4b**). The sub-nanometer metal clusters are posited to be alloyed due to the close vicinity of gold and copper in the precursor ions; however, in this case it was not possible to

directly confirm whether the clusters were mono- or multimetallic. Interestingly, oxidizing the metal thiolate precursors to monometallic ions with hydrogen peroxide followed by chemical reduction by sodium borohydride, formed aggregated polydisperse nanoparticles that were predominantly gold with little copper alloying (**Fig. 4c,d**). This result echoes that observed with high dose rate LPTEM and suggests a common chemical mechanism explaining the preferential gold reduction in both the *in situ* and *ex situ* syntheses. The strongly oxidizing environment of the high dose LPTEM imaging experiment, simulated by addition of hydrogen peroxide in the bench scale experiment, breaks down metal thiolate precursors that are critical to formation of AuCu alloys (**Fig. 4e**). This work demonstrates the power of utilizing LPTEM together with solution chemistry and chemical analysis to deduce the chemical mechanisms underlying the role of metal-ligand complexes in forming alloyed nanoparticles.

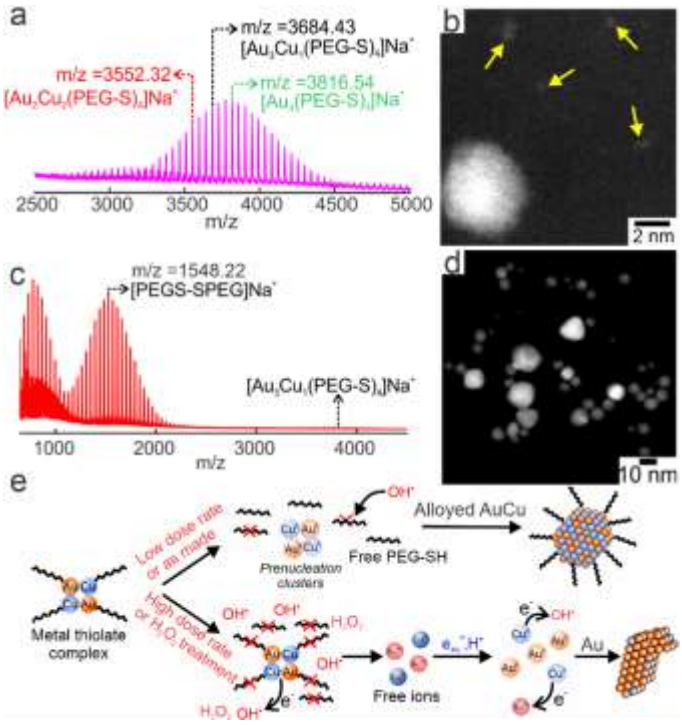

Fig. 4. Establishing the role of multimetallic metal thiolate precursors on alloying and formation mechanism of AuCu nanoparticles. (a) MALDI-TOF spectrum of as made metal thiolate precursor

species containing gold and copper sites. (b) HAADF-STEM image showing AuCu nanoparticles formed from metal thiolate precursors co-existed with subnanometer metal cluster intermediates. (c) MALDI-TOF spectra of the metal thiolate precursor after exposing metal thiolates to hydrogen peroxide for 24 hours. (d) HAADF-STEM image of nanoparticles formed from oxidized metal thiolates. (e) Cartoon schematic demonstrating the formation mechanism of AuCu and Au nanoparticles during LPTEM and solution chemical synthesis. Adapted with permission from *ACS Nano*, 2021, **15**, 2578-2588. Copyright 2021 American Chemical Society.

3.2. Formation mechanism and dynamics of high entropy alloy nanoparticles

High entropy alloy (HEA) nanoparticles consist of five or more metals present in near equimolar proportions and stabilized by high mixing entropy.[92,93] Prior work has suggested that HEA nanoparticles form by classical nucleation and growth mechanisms following Lamer's model, but there remains a lack of dedicated mechanistic studies.[13,94,95] Prior work in section 2.2 demonstrated that LPTEM can produce radiolysis synthesis conditions that resemble solution chemistry synthesis, which allowed investigated the formation mechanism of HEA nanoparticles by LPTEM.[59] Sun *et al.* used systematic solution chemistry to synthesize HEA nanoparticles from a mixture of metal salts and PEG-SH, together with LPTEM to understand the formation mechanism.[7] Interestingly, the HEA nanoparticles formed by solution chemistry here were found to co-exist with stable sub-nanometer clusters and free metal atoms as shown in **Fig. 5a.** MALDI-TOF MS of the metal clusters indicated they were multimetallic, which suggested that HEA alloy formation began at the molecular level (**Fig. 5b**). HEA particle size increased with increasing sodium borohydride concentration, which together with the stable single atoms and metal clusters in the reaction solution suggested that classical nucleation and monomer attachment was not the

formation mechanism. LPTEM generated radicals were utilized as strong reducing agents to synthesize HEA nanoparticles and produced alloyed nanoparticles with similar composition to those formed by wet synthesis. The growth kinetics of the HEA nanoparticles displayed power law growth with an exponent of $t^{1/3}$ (**Fig. 5c**). Analysis of the particle size distribution shape and comparison to various growth models suggested that nanoparticle growth was dominated by aggregation processes instead of diffusion limited growth. LPTEM studies on mixtures of preformed HEA nanoparticles and sub-nanometer clusters with no metal ions in solution showed that ligand displacement from the sub-nanometer clusters facilitated self-growth (yellow arrows) and aggregative growth of HEA nanoparticles (white, blue, and green arrows) (**Fig. 5d**). Taken together, these experiments supported an HEA formation mechanism involving ligand desorption-induced aggregation of multimetallic clusters (**Fig. 5e**).[7] Here, the rate limiting step during nanoparticle formation is diffusion limited aggregation of clusters in solution, as opposed to nucleation of nanoparticle seeds. Importantly, aggregation of metal cluster intermediates mitigates the problem of preferential reduction of certain metals by promoting mixing of different metal species. HEA nanoparticle formation by aggregation is analogous to synthesizing kinetically trapped nanoparticles with high index facets and surface energies *via* nucleation and growth at very high supersaturation.[96] In this case, rapid aggregation of metal cluster intermediates at high supersaturation enables mixing metal species that are not nominally soluble to form a non-equilibrium HEA structure. This work highlighted the existence and important role of sub-nanometer metal clusters during the HEA synthesis in colloidal phase and suggests paths for future multi-metallic or HEA nanoparticle synthesis by rational control of intermediate metal clusters.

Erni and co-workers investigated nanoparticle coalescence-based growth mechanisms using GLC-TEM to visualize nanoparticle formation at the atomic scale.[33,97–100] They observed

that metal atom aggregation into metal clusters played a vital role in facilitating attachment-based growth of PtPd nanoparticles (**Fig. 5f**).[33] They identified amorphous and crystalline metal clusters that aggregated to form alloyed PtPd nanoparticles. Amorphous metal clusters were observed to undergo self-crystallization. Likewise, the nucleation dynamics of Pd nanoparticles was further studied by GLC-TEM as shown by **Fig. 5g**.[100] Initially, Pd atom aggregation formed amorphous metal clusters, which continuously aggregated and coalesced to form large amorphous particles. Finally, the amorphous particles crystallized with defined facets. This work quantitively studied particle nucleation kinetics and coalescence steps (**Fig. 5h**), which effected a significant decrease in particle number and increase in particle size that was counter to Lamer's classic model. These studies emphasized that multi-step nanoparticle growth mechanisms including single atom and metal cluster aggregation are critical to controlling the composition and size of metal nanoparticles. Together, the works of the Erni lab and Woehl lab provide direct visualize evidence for the proposed metal cluster aggregation-based mechanism proposed by Polte *et al.*[10]

A recent study by Shahbazian-Yassar *et al.* investigated the interaction between multi-metallic nanoparticles and bacteria by GLC-TEM (**Fig. 5i**). The authors posited that electron transfer from the nanoparticles to the bacteria caused metal cation release.[101] Direct GLC-TEM observations found that the binding affinity of bacteria surface functional groups to different metal cations led to varying degrees of metal cation release and surface diffusion. The metal cations were released at a faster rate when there was higher binding affinity between the metal cations and the bacterial proteins.

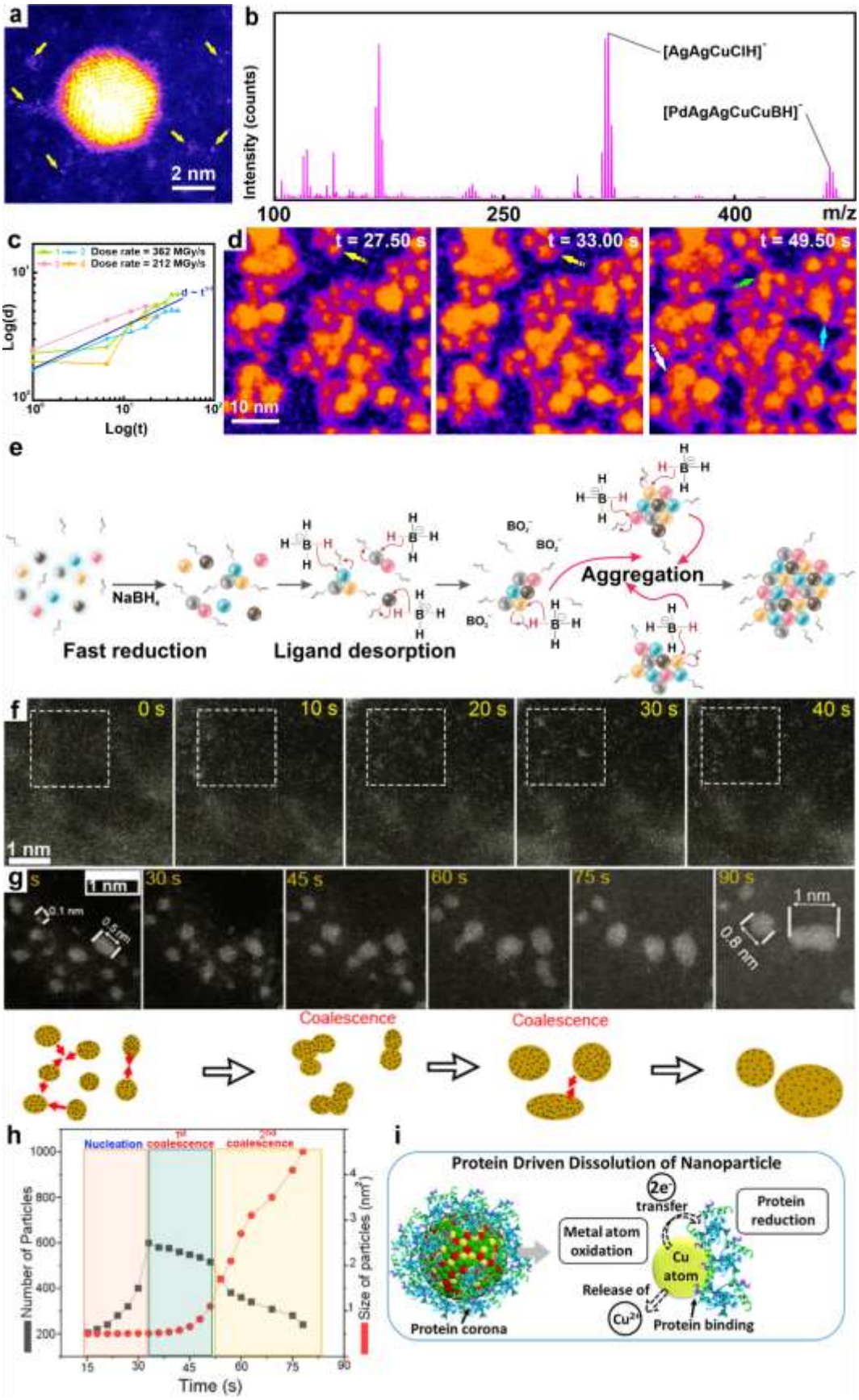
a
2 nm
b
Intensity (counts)
[AgAgCuClH]⁻
[PdAgAgCuCuBH]⁻
100
250
400
m/z
c
Dose rate = 362 MGy/s
Dose rate = 212 MGy/s
Log(d)
Log(t)
d
t = 27.50 s
t = 33.00 s
t = 49.50 s
10 nm
e
NaBH4
Fast reduction
Ligand desorption
Aggregation
f
0 s
10 s
20 s
30 s
40 s
1 nm
g
s
1 nm
0.1 nm
0.5 nm
30 s
45 s
60 s
75 s
90 s
1 nm
0.8 nm
Coalescence
Coalescence
h
Nucleation
1st coalescence
2nd coalescence
Number of Particles
Size of particles (nm²)
Time (s)
i
Protein Driven Dissolution of Nanoparticle
2e⁻ transfer
Protein reduction
Metal atom oxidation
Cu atom
Release of Cu²⁺
Protein binding
Protein corona

Fig. 5. Aggregation-based nonclassical growth of nanoparticles revealed by LPTEM studies. (a) HAADF-STEM image of an HEA nanoparticle surrounded by sub-nanometer clusters and single atoms. The image is false colored and contrast adjusted to highlight the clusters and atoms (yellow arrows). (b) MALDI-TOF MS spectrum of metal clusters in an HEA nanoparticle solution. (c) Diameter of individual HEA nanoparticles as a function of time from LPTEM movies plotted on a logarithmic scale. The nanoparticle diameters increase as $d \sim t^{1/3}$, as shown by the solid line. (d) Time-lapsed LPTEM images showing growth and aggregation of preformed HEA nanoparticles with no metal precursor present at a magnification of 1,500,000 × (beam current = 74 pA, dose rate = 682 MGy/s). The images have been cropped and false colored to highlight aggregation of small nanoparticles and clusters. Arrows denote examples of aggregative growth. (e) Aggregative reaction mechanism for HEA nanoparticle formation. (a)-(e) Adapted with permission from *Nanoscale*, 2023, **15**, 10447-10457. Copyright 2021 Royal Society of Chemistry. (f) Time-lapse series of atomic resolution HAADF-STEM images show the formation of Pt and Pd nanoclusters in liquid. Adapted with permission from *ACS Nano*, 2022, **16**, 14198–14209. Copyright 2022 American Chemical Society. (g) Top: Time-lapse series of atomic resolution HAADF-STEM images showing a group of Pd nanoclusters undergoing coalescence to form amorphous Pd nanoparticles. Bottom: Corresponding schematic illustration. (h) Average Pd particles size evolution (red) and the number of particles (blue) as a function of time. (g)-(h) Adapted with permission from *Chem. Mater.* 2023, **35**, 1201–1208. Copyright 2023 American Chemical Society. (i) Schematic representation of protein driven oxidative dissolution of nanoparticles. Adapted with permission from *ACS Nano* 2023, **17**, 5880–5893. Copyright 2023 American Chemical Society.

3.3. Distinguishing between radiolysis and plasmonic induced metal deposition on plasmonic nanorods

Aside from chemical stimuli, colloidal nanoparticle synthesis can be stimulated using optical phenomena. Under appropriate conditions, collective oscillations of conduction band electrons known as localized surface plasmon resonances (LSPRs) are excited in metallic nanoparticles by visible light.[102–107] LSPR produces electric field enhancement near the particle surface. LSPR excitation is rapidly (within 10^{-15} to 10^{-12} s) followed by damping resulting in radiation, heating, or formation of excited charge carriers, *i.e.*, "hot" electrons and holes, near the nanoparticle surface.[108–112] Accordingly, plasmonic nanoparticles can promote surface redox or thermally-activated chemical reactions.[105,106,113–115] Hot electrons originating in plasmonic nanoparticles can be harnessed to deposit secondary metal shells, as shown by work from Ortiz *et al.* and Forcherio *et al.*[106,115–117] In these cases, the secondary metals deposited preferentially at the tips of the AuNRs due to excitation of the longitudinal LSPR. Mechanistic details of this process are poorly understood, including the rate of hot electron generation, hot electron energy distribution, and the spatial distribution of hot electron generation across the nanorod surface. Multiple groups have leveraged LPTEM to visualize metal deposition dynamics on metal nanoparticle seeds in real time, albeit utilizing radiolysis as the stimulus.[42,63,64] Furthermore, previous studies using STEM-EELS demonstrated the electron beam can excite both bright and dark LSPR modes within metallic nanoparticles.[104,118,119] Sutter *et al.* indicated that the STEM beam acts as a localized evanescent white light source and posited that hot electrons and field enhancement drives nanoparticle growth and shape transformation during LPTEM imaging.[120,121] The observations were made in aqueous solution containing Ag^+ precursor and sodium citrate,

similar to prior work by Jin *et al.* demonstrating plasmon-mediated transformation of spherical Ag seed particles to nanoprisms in light-irradiated solution.[112,122–125]

Altogether, LPTEM is a promising tool to extend insight into secondary metal reduction by plasmonic hot electrons, motivating recent work by Chen *et al.* to examine Ag deposition onto cetyltrimethylammonium bromide (CTAB) capped AuNRs (**Fig. 6a**).[126] While the electron beam may stimulate Ag^+ reduction by AuNR plasmonic hot electrons, water also produces various radicals capable of reducing Ag under electron irradiation (*cf.* Section 2.1).[48,50,55,127] As such, this work sought to clarify the relative contributions of hot electron driven and radiolysis driven silver reduction onto AuNRs during LPTEM. In the presence of different CTAB concentrations, silver deposited onto AuNRs in either faceted bipyramidal shells or tip-preferential lobes (**Figs. 6b-e**). Furthermore, silver avoided depositing in narrow spaces between adjacent AuNRs (see areas marked in **Figs. 6d,e**). Companion *ex situ* photodeposition experiments utilizing methanol as a hole scavenger showed preferential deposition of Ag in narrow gaps between closely spaced AuNRs, agreeing with simulated locations of hot electron generation hot spots (**Fig. 6f-i**).[114,106,116,117,128,129] In view of previous work by Aliyah *et al.* demonstrating metal shell deposition on gold nanoparticle seeds during LPTEM occurred via a similar growth mechanism as *ex situ* chemical reduction by ascorbic acid (AA), Chen *et al.* conducted additional *ex situ* experiments utilizing AA as a chemical reductant.[63] As seen in **Figs. 6j-m**, *ex situ* synthesis experiments identified conditions producing pyramidal or tip-selective shell morphologies resembling the modes observed *in situ* with LPTEM. Furthermore, at most CTAB concentrations examined, similar shell morphologies were obtained by applying chemical reduction with or without photoexcitation. Overall, systematic *ex situ* experiments along with plasmonic simulations enabled disambiguating the relative contributions of chemical versus plasmonic hot electron reduction

during LPTEM. Taken together, these results were consistent with metal deposition *via* chemical reduction by radiolytic radicals. While the silver lobe morphology observed during LPTEM is reminiscent of LSPR electric field enhancement, the solution chemistry experiments demonstrated this effect was due to preferential ligand removal from the AuNR tips.

3.4. Probing metal shell deposition on nanoparticles using LPTEM and correlative methods

One key insight from our work is that minimizing the presence of chemically reducing species is required to isolate plasmonic hot electron reduction, a prospect which will be further discussed later. Notably, correlative experiments and modeling were central to interpreting LPTEM observations and evaluating the suitability of LPTEM to probe plasmon-driven redox processes. Similar approaches have been followed in other LPTEM studies of plasmonic nanoparticle systems. In addition to LPTEM, Aliyah *et al.* utilized UV-vis spectroscopy and small angle X-ray scattering (SAXS) to monitor ensemble morphological evolution *in situ* under conditions more closely related to benchtop synthesis.[63] Data furnished by these techniques complemented visual LPTEM observations, leading to novel insights showing that AA acts as a facet-directing adsorbate during Ag shell deposition. As seen in **Fig. 7a**, LPTEM showed that Ag deposited onto the Au seeds in the presence of AA and CTAC (cetyltrimethylammonium chloride) to form high aspect ratio nanorods with tips terminated by {111} facets. TEM and UV-VIS results from accompanying bulk synthesis experiments (**Fig. 7b-g**) revealed that AA and halide ions were both necessary to obtain this particle morphology. While Sutter *et al.* also employed complementary *ex situ* synthesis in conjunction with UV-vis spectroscopy, there was greater emphasis on plasmonic simulations for comparison and interpretation of LPTEM results.[120,121] **Fig. 7h** shows LPTEM observations of triangular Ag nanoprism growth around a seed particle, with

edge-flow growth being especially apparent from 34-51 s. **Fig. 7i** shows a map of simulated field enhancement due to LSPR for a relevant particle configuration. While these results are interesting and indeed suggest relevance to the LPTEM observations, the work by Chen *et al.* demonstrates that in some cases radiation chemistry can overshadow plasmon-driven effects during LPTEM, confounding efforts to observe plasmon-mediated redox processes.[126]

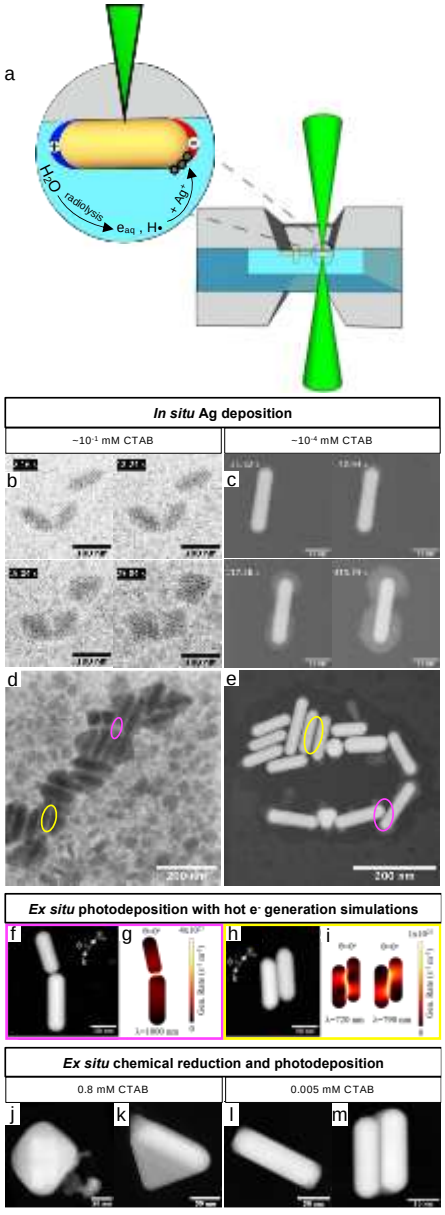

Fig. 6. **a**) Schematic of simultaneous *in situ* chemical reduction and plasmonic hot electron reduction of Ag onto AuNRs during LPTEM. **b,c**) Time-lapsed images of *in situ* faceted bipyramidal Ag shell growth (BF-STEM) and tip-selective Ag lobe growth (HAADF-STEM) respectively. **d,e**) Aggregated AuNRs after Ag deposition in the presence of ~10^{-1} mM CTAB (BF-STEM image) and ~10^{-4} mM CTAB (HAADF-STEM image), respectively. Ovals mark exemplary interfaces between rods aligned side-by-side (yellow) or end-to-end (magenta). **f-i**) HAADF-STEM images showing pairs of AuNRs arranged either end-to-end or side-by-side observed after *ex situ* Ag photodeposition experiments, along with corresponding simulated hot electron generation maps of select LSPR modes. **j-m**) HAADF-STEM images of paired or individual AuNRs observed after *ex situ* experiments applying chemical reduction along with photoexcitation. Adapted with permission from *J. Phys. Chem. Lett.*, 2023, **14**, 1379-1388.

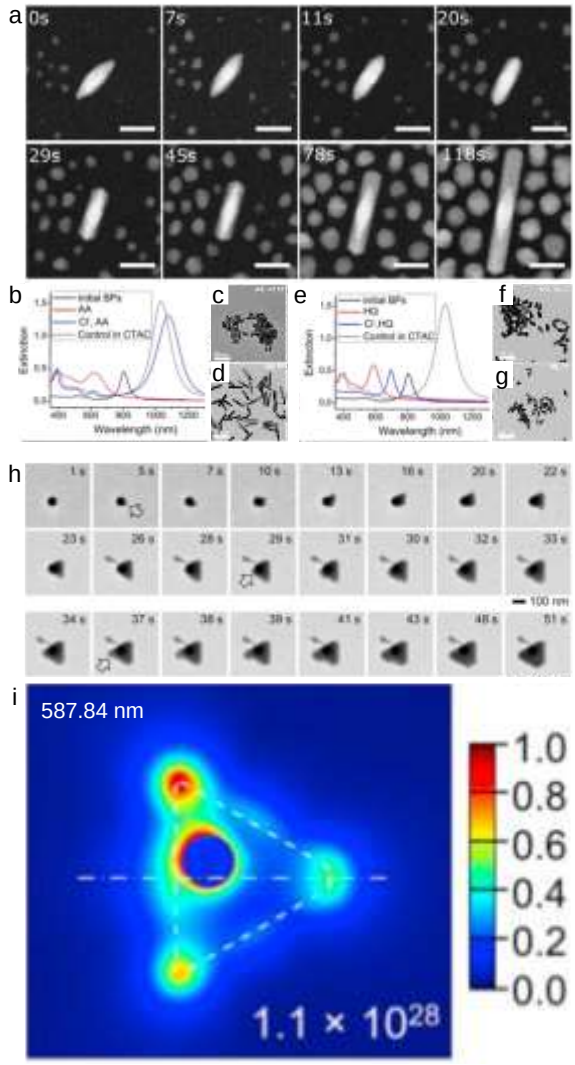

Fig. 7. LPTEM imaging of metal deposition and shape transformation of plasmonic nanoparticles. **a**) Time-lapsed STEM images of Ag deposition onto a pentatwinned bipyramidal (BP) Au seed observed during LPTEM. The scale bar in each frame is 50 nm. **b-d**) UV-vis extinction spectra of particles synthesized using AA with or without Cl^-, along with corresponding TEM images. **e-g**) UV-vis extinction spectra of particles synthesized using hydroquinone (HQ) as the chemical reductant, with or without Cl^-, along with corresponding TEM images. (a)-(g) adapted with permission from *J. Phys. Chem. Lett.*, 2020, **11**, 2830-2837. Copyright 2020 American Chemical Society. **h**) Time-lapsed STEM images of triangular Ag nanoprism growth around a Ag seed

particle during LPTEM. Arrows in select frames mark the starting positions of growing edges. **i**) Simulated LSPR electric field distribution ($|E/E_{Max}|$) for a Ag nanoprism with spherical particle embedded off the symmetry axis. (h-i) adapted with permission from *J. Amer. Chem. Soc*., 2017, **139**, 6771-6776. Copyright 2017 American Chemical Society.

4. Conclusions and outlook

4.1. Probing molecular scale intermediates with flow LPTEM

There has been remarkable progress in utilizing LPTEM to visualize formation of nanoparticles at the nanometer and atomic scale, but molecular intermediates remain beyond the resolving power of this technique. The molecular structure, including bonding, oxidation state, molecular weight, crystallinity, and composition, of these intermediates remains mysterious for most nanoparticle syntheses. Recent work by the Jones lab demonstrating the importance of atomically precise metal nanoclusters in seeded nanoparticle synthesis emphasizes the need to consider the molecular structure of intermediate species when developing growth mechanisms for nanoparticles.[130] While studies of bimetallic and HEA nanoparticle revealed sub-nanometer metal clusters in the reaction solution following synthesis,[7,59] these species were below the LPTEM spatial resolution so it could not be verified these clusters were indeed intermediates to the final crystalline nanoparticles. Future research should focus on detecting and characterizing metal cluster reaction intermediates during LPTEM experiments and drawing concrete connections between these intermediates and the nanoparticle formation dynamics. Due to its high sensitivity and small required sample volume (~μL), mass spectrometry is a promising technique for analyzing molecular species formed during LPTEM. The Gianneschi lab has demonstrated

MALDI TOF IMS to be an invaluable technique for evaluating electron beam damage to organic molecules during LPTEM,[88] demonstrating feasibility of this approach. Emerging technologies, such as microfluidic and nanofluidic liquid TEM sample cells with well-defined channel geometries and fluid flow will enable reliable continuous flow LPTEM experiments.[131,132] Capturing irradiated liquid will enable mass spectrometry characterization of the molecular weight and molecular structure of reaction intermediates. Well-defined fluidic channels in the sample holder will enable pseudo-real time or even real time measurements of molecular species that are correlated in time with *in situ* LPTEM movies. For instance, by utilizing this flow microscopy approach, we anticipate measuring the mass spectra of metal nanoparticle reaction intermediates, such as ligand-protected metal clusters, that are challenging to detect and isolate during wet chemical synthesis. Understanding the chemical identity and molecular weight of reaction intermediates will enable constructing formation mechanisms and quantitative kinetic models that are consistent with *both the nanoscale LPTEM observations and the molecular reaction intermediates*. One anticipated challenging of using flow microscopy to collect intermediate species generated by electron beam radiolysis is the stability of the intermediates and whether they will change between the LPTEM experiment and chemical analysis. A tandem mass spectrometry/LPTEM system could alleviate the lag time between sample collection and chemical analysis but would represent a significant technological and engineering challenge. We expect that this approach of correlative real time chemical analysis and LPTEM will propel LPTEM beyond the current restraints of pure visual observation.

4.2. Isolating plasmon driven redox processes during LPTEM

The work by Chen *et al.* discussed above[126] suggests that isolating and observing plasmonic hot carrier-driven redox processes *via* LPTEM will require minimizing chemically reactive radical formation, which can potentially be realized using radiation resistant organic solvents. Abellan *et al.* observed no chemical reduction or other apparent beam induced processes occurring within over 15 minutes of electron beam exposure of lithium triflate in dimethyl sulfoxide (DMSO).[133] Similarly, Abellan *et al.* and Bhattarai *et al.* leveraged the low radical generation rates in toluene to exert control over Pd nanoparticle growth kinetics and PbTe nanoparticle etching, respectively.[134,135] The aromatic structure of toluene imparts resonance stabilization and makes this solvent especially resilient towards electron irradiation, resulting in fewer possible radical products with lower G-values.[136,137] The primary reactive species of concern for toluene is H_2,[138] which can function as a reductant and has a G-value of 0.14 molecules/100 eV.[134] In contrast, reported G-values of e^-_{aq} and $H^{\cdot}$ in water are 2.6 and 0.55 molecules/100 eV.[127] While toluene possesses promising qualities to suppress generation of reactive species, it must be noted that residual trace water from specimen preparation can unfavorably impact the chemistry if not carefully mitigated.[135] Addressing such challenges is expected to enable LSPR hot carriers to dominate observed redox processes in LPTEM. Other challenges of using apolar aromatic solvents include limitations in the types of solutes that can be utilized, including the metal salts typically used for metal nanoparticle synthesis. Likewise, a common hole scavenger used in metal photodeposition on plasmonic metal nanoparticles is sodium citrate, which is not soluble in apolar aromatic solvents. Therefore, this approach will require additional *ex situ* photodeposition experiments to identify suitable metal precursors and hole scavengers.

4.3. Beyond electron beam driven nanoparticle formation during LPTEM

The electron beam remains the primary stimulus for driving nanoparticle formation during LPTEM. Despite several works establishing similarity between LPTEM and wet chemical synthesis reaction conditions,[59,63] the use of exotic radicals to stimulate nanoparticle growth leaves open the question of whether this approach can bring valuable insights into solution chemistry reactions. Microfluidic flow sample cells enable introducing liquid chemical reductants,[139] but laminar flow in the micron sized fluid channels prevents rapid mixing similar to wet chemical synthesis. An alternative approach enabled by the advent and commercialization of liquid heating sample holders for LPTEM is thermally driven nanoparticle synthesis. Here reducing agent is generated *in situ* by increasing temperature, which circumvents the need to inject and mix a separate chemical reductant. Polyol synthesis and hot injection synthesis represent two major classes of thermal nanoparticle synthesis for metallic and semiconductor nanoparticles, respectively.[140,141] In particular, polyol synthesis utilizes diols, such as ethylene glycol, as the solvent and reducing agent. Heating the precursor to temperatures between 100 – 200 °C causes the diol to become increasingly reducing in nature, effectively generating reducing agent *in situ*. Recent works by the Alloyeau and Ross labs have begun to establish the impact of sample temperature on electron beam induced nanoparticle formation during LPTEM.[142,143] These important works set the foundation for future work that utilizes heating at the primary stimulus for nanoparticle synthesis during LPTEM. Finally, hydrothermal synthesis is a widely used synthetic method for complex metal oxides, which utilizes conditions that are currently out of reach for MEMS based liquid cells. Specifically, the high pressures and temperatures reached during hydrothermal synthesis exceed the limits of current commercial MEMS based systems. Given the importance of complex metal oxides for lithium-ion battery cathodes, development of high temperature, high pressure MEMS devices capable of creating hydrothermal synthesis conditions

represents an important research direction for LPTEM. With the common use of *in situ* heating cells for other analytical techniques, such as *in situ* UV-VIS and small angle x-ray scattering (SAXS), thermal synthesis provides a unique opportunity for combining multiple in situ characterization techniques to probe nanoparticle growth mechanisms.

Recent technological developments have enabled illuminating liquid samples with light during LPTEM, which is a potential novel approach to investigate LSPR induced phenomena in plasmonic nanoparticles. This approach combines the advantages of the high spatial resolution of the electron beam with use of a more commonly accepted stimulus for LSPR-mediated phenomena. Specialized stages that support optical fibers can subject fluid samples to *in situ* laser illumination,[144] while fiber optic coupled sample drive lasers have been utilized for over a decade in dynamic TEM (DTEM) instruments. Pump-probe laser systems integrated into the TEM can enable ultrafast temporal resolution of dynamics initiated by optical stimuli (down to picoseconds).[145–148] This is achieved through a dual-laser optical system, with one laser illuminating the sample (pump) while the other excites the electron source (probe). For instance, Fu *et al.* leveraged such an apparatus to study explosive boiling of water near the surface of gold nanoparticles due to rapid plasmon-induced localized heating, which nucleated steam bubbles that could migrate, coalesce, expand, or collapse, propelling the nanoparticles in the process.[146] Recent work by Liu and Arslan *et al.* utilized photon-induced near-field electron microscopy in a DTEM instrument to capture plasmonic coupling with nanometer scale spatial resolution and picosecond temporal resolution.[149] These recent technological advancements, together with their commercialization in TEM platforms, are expected to open the door to investigating metal photodeposition on plasmonic nanoparticles and other related LSPR phenomena.

Acknowledgements

This material is based upon work supported by the National Science Foundation under grant no. 2045258. We thank Dr. S. C. Liou and Dr. W. A. Chiou for their assistance with electron microscopy work.

CRediT authorship contribution statement

Amy Chen: formal analysis, writing – original draft, writing – review & editing, visualization. **Thilini Dissanayake**: formal analysis, writing – original draft, writing – review & editing, visualization. **Jiayue Sun**: formal analysis, writing – original draft, writing – review & editing, visualization. **Taylor Woehl**: Conceptualization, formal analysis, writing – original draft, writing – review & editing, visualization, supervision, funding acquisition.

References

1 K. Park, L. F. Drummy, R. C. Wadams, H. Koerner, D. Nepal, L. Fabris and R. A. Vaia, *Chem. Mater.*, 2013, **25**, 555–563.
2 M. Wuithschick, A. Birnbaum, S. Witte, M. Sztucki, U. Vainio, N. Pinna, K. Rademann, F. Emmerling, R. Kraehnert and J. Polte, *ACS Nano*, 2015, **9**, 7052–7071.
3 S. Seibt, H. Zhang, S. Mudie, S. Förster and P. Mulvaney, *J. Phys. Chem. C*, 2021, **125**, 19947–19960.
4 M. Sun, Z. Cheng, W. Chen and M. Jones, *ACS Nano*, 2021, **15**, 15953–15961.
5 Q. Yao, X. Yuan, V. Fung, Y. Yu, D. T. Leong, D. Jiang and J. Xie, *Nature Comm.*, 2017, **8**, 927.
6 A. Loiudice and R. Buonsanti, *Nature Synth.*, 2022, **1**, 344–351.
7 J. Sun, A. Leff, Y. Li and T. J. Woehl, *Nanoscale*, 2023, **15**, 10447–10457.
8 G. R. Dey, C. R. McCormick, S. S. Soliman, A. J. Darling and R. E. Schaak, *ACS Nano*, 2023, **17**, 5943–5955.
9 R. Xie, Z. Li and X. Peng, *J. Am. Chem. Soc.*, 2009, **131**, 15457–15466.
10 M. Wuithschick, S. Witte, F. Kettemann, K. Rademann and J. Polte, *Phys. Chem. Chem. Phys.*, 2015, **17**, 19895–19900.
11 J. S. Kim, H. Chang, S. Kang, S. Cha, H. Cho, S. J. Kwak, N. Park, Y. Kim, D. Kang, C. K. Song, J. Kwag, J.-S. Hahn, W. B. Lee, T. Hyeon and J. Park, *Nature Commun.*, 2023, **14**, 3201.
12 Y. Cao, J. Guo, R. Shi, G. I. N. Waterhouse, J. Pan, Z. Du, Q. Yao, L.-Z. Wu, C.-H. Tung, J. Xie and T. Zhang, *Nat. Commun.*, 2018, **9**, 2379.

13 Y. Yao, Z. Huang, P. Xie, S. D. Lacey, R. J. Jacob, H. Xie, F. Chen, A. Nie, T. Pu, M. Rehwoldt, D. Yu, M. R. Zachariah, C. Wang, R. Shahbazian-Yassar, J. Li and L. Hu, *Science*, 2018, **359**, 1489–1494.

14 P.-C. Chen, J. S. Du, B. Meckes, L. Huang, Z. Xie, J. L. Hedrick, V. P. Dravid and C. A. Mirkin, *J. Am. Chem. Soc.*, 2017, **139**, 9876–9884.

15 L. Huang, H. Lin, C. Y. Zheng, E. J. Kluender, R. Golnabi, B. Shen and C. A. Mirkin, *J. Am. Chem. Soc.*, 2020, **142**, 4570–4575.

16 W.-T. Koo, J. E. Millstone, P. S. Weiss and I.-D. Kim, *ACS Nano*, 2020, **14**, 6407–6413.

17 M. A. Wall, B. M. Cossairt and J. T. C. Liu, *J. Phys. Chem. C*, 2018, **122**, 9671–9679.

18 M. J. Williamson, R. M. Tromp, P. M. Vereecken, R. Hull and F. M. Ross, *Nat. Mater.*, 2003, **2**, 532–536.

19 N. de Jonge and F. M. Ross, *Nat. Nanotechnol.*, 2011, **6**, 695–704.

20 F. M. Ross, *Science*, 2015, **350**, aaa9886.

21 H. Zheng, R. K. Smith, Y. Jun, C. Kisielowski, U. Dahmen and A. P. Alivisatos, *Science*, 2009, **324**, 1309–1312.

22 J. M. Yuk, J. Park, P. Ercius, K. Kim, D. J. Hellebusch, M. F. Crommie, J. Y. Lee, A. Zettl and A. P. Alivisatos, *Science*, 2012, **336**, 61–64.

23 H.-G. Liao, K. Niu and H. Zheng, *Chem. Commun.*, 2013, **49**, 11720–11727.

24 D. Li, M. H. Nielsen, J. R. I. Lee, C. Frandsen, J. F. Banfield and J. J. De Yoreo, *Science*, 2012, **336**, 1014–1018.

25 T. J. Woehl, J. E. Evans, I. Arslan, W. D. Ristenpart and N. D. Browning, *ACS Nano*, 2012, **6**, 8599–8610.

26 J. H. Park, N. M. Schneider, J. M. Grogan, M. C. Reuter, H. H. Bau, S. Kodambaka and F. M. Ross, *Nano Lett.*, 2015, **15**, 5314–5320.

27 D. Alloyeau, W. Dachraoui, Y. Javed, H. Belkahla, G. Wang, H. Lecoq, S. Ammar, O. Ersen, A. Wisnet, F. Gazeau and C. Ricolleau, *Nano Lett.*, 2015, **15**, 2574–2581.

28 M. Wang, T. Dissanayake, C. Park, K. Gaskell and T. Woehl, *J. Amer. Chem. Soc.*, 2019, **141**, 13516–13524.

29 B. K. Choi, J. Kim, Z. Luo, J. Kim, J. H. Kim, T. Hyeon, S. Mehraeen, S. Park and J. Park, *ACS Nano*, 2023, **17**, 2007–2018.

30 N. Ahmad, G. Wang, J. Nelayah, C. Ricolleau and D. Alloyeau, *Nano Lett.*, 2017, **17**, 4194–4201.

31 N. D. Loh, S. Sen, M. Bosman, S. F. Tan, J. Zhong, C. A. Nijhuis, P. Král, P. Matsudaira and U. Mirsaidov, *Nat. Chem.*, 2017, **9**, 77–82.

32 B. Jin, Y. Wang, Z. Liu, A. France-Lanord, J. C. Grossman, C. Jin and R. Tang, *Adv. Mater.*, 2019, **31**, 1808225.

33 W. Dachraoui, M. I. Bodnarchuk and R. Erni, *ACS Nano*, 2022, **16**, 14198–14209.

34 C. Zhu, S. Liang, E. Song, Y. Zhou, W. Wang, F. Shan, Y. Shi, C. Hao, K. Yin, T. Zhang, J. Liu, H. Zheng and L. Sun, *Nat. Commun.*, 2018, **9**, 421.

35 Y. Bae, K. Lim, S. Kim, D. Kang, B. H. Kim, J. Kim, S. Kang, S. Jeon, J. Cho, W. B. Lee, W. C. Lee and J. Park, *Nano Lett.*, 2020, **20**, 8704–8710.

36 G. Li, N. He, J. Deng, J. Liu, Y. Sun, M. Qu, Y. Jiang, T. Zhao, S.-Y. Zhou, H. Zeng, Q. Zheng, H.-G. Liao and S.-G. Sun, *Cryst. Growth Des.*, 2021, **21**, 6025–6030.

37 H.-G. Liao, L. Cui, S. Whitelam and H. Zheng, *Science*, 2012, **336**, 1011–1014.

38 D. J. Kelly, M. Zhou, N. Clark, M. J. Hamer, E. A. Lewis, A. M. Rakowski, S. J. Haigh and R. V. Gorbachev, *Nano Lett.*, 2018, **18**, 1168–1174.

39 C. Wang, Q. Qiao, T. Shokuhfar and R. F. Klie, *Adv. Mater.*, 2014, **26**, 3410–3414.

40 J. J. Calvin, A. S. Brewer and A. P. Alivisatos, *Nat. Synth.*, 2022, **1**, 127–137.

41 N. de Jonge, L. Houben, R. E. Dunin-Borkowski and F. M. Ross, *Nat. Rev. Mater.*, 2019, **4**, 61–78.

42 A. Hutzler, T. Schmutzler, M. P. M. Jank, R. Branscheid, T. Unruh, E. Spiecker and L. Frey, *Nano Lett.*, 2018, **18**, 7222–7229.

43 N. Clark, D. J. Kelly, M. Zhou, Y.-C. Zou, C. W. Myung, D. G. Hopkinson, C. Schran, A. Michaelides, R. Gorbachev and S. J. Haigh, *Nature*, 2022, **609**, 942–947.

44 J. Park, H. Elmlund, P. Ercius, J. M. Yuk, D. T. Limmer, Q. Chen, K. Kim, S. H. Han, D. A. Weitz, A. Zettl and A. P. Alivisatos, *Science*, 2015, **349**, 290–295.

45 J. Yang, Z. Zeng, J. Kang, S. Betzler, C. Czarnik, X. Zhang, C. Ophus, C. Yu, K. Bustillo, M. Pan, J. Qiu, L.-W. Wang and H. Zheng, *Nat. Mater.*, 2019, **18**, 970–976.

46 J. Hong, J.-H. Bae, H. Jo, H.-Y. Park, S. Lee, S. J. Hong, H. Chun, M. K. Cho, J. Kim, J. Kim, Y. Son, H. Jin, J.-Y. Suh, S.-C. Kim, H.-K. Roh, K. H. Lee, H.-S. Kim, K. Y. Chung, C. W. Yoon, K. Lee, S. H. Kim, J.-P. Ahn, H. Baik, G. H. Kim, B. Han, S. Jin, T. Hyeon, J. Park, C. Y. Son, Y. Yang, Y.-S. Lee, S. J. Yoo and D. W. Chun, *Nature*, 2022, **603**, 631–636.

47 G. R. Dey, C. R. McCormick, S. S. Soliman, A. J. Darling and R. E. Schaak, *ACS Nano*, 2023, **17**, 5943–5955.

48 T. Woehl and P. Abellan, *J. Microsc.*, 2017, **265**, 135–147.

49 T. Woehl, T. Moser, J. Evans and F. Ross, *MRS Bulletin*, 2020, **45**, 746–753.

50 T. J. Woehl, *Chem. Mater.*, 2020, **32**, 7569–7581.

51 B. Fritsch, T. S. Zech, M. P. Bruns, A. Körner, S. Khadivianazar, M. Wu, N. Zargar Talebi, S. Virtanen, T. Unruh, M. P. M. Jank, E. Spiecker and A. Hutzler, *Adv. Sci.*, 2022, **9**, 2202803.

52 J. Lee, D. Nicholls, N. D. Browning and B. L. Mehdi, *Phys. Chem. Chem. Phys.*, 2021, **23**, 17766–17773.

53 S. Merkens, G. De Salvo and A. Chuvilin, *Nano Express*, 2023, **3**, 045006.

54 B. Fritsch, A. Körner, T. Couasnon, R. Blukis, M. Taherkhani, L. G. Benning, M. P. M. Jank, E. Spiecker and A. Hutzler, *J. Phys. Chem. Lett.*, 2023, **14**, 4644–4651.

55 N. M. Schneider, M. M. Norton, B. J. Mendel, J. M. Grogan, F. M. Ross and H. H. Bau, *J. Phys. Chem. C*, 2014, **118**, 22373–22382.

56 J. Korpanty, K. Gnanasekaran, C. Venkatramani, N. Zang and N. C. Gianneschi, *Cell Rep. Phys. Sci.*, 2022, **3**, 100772.

57 M. S. Matheson, A. Mamou, J. Silverman and J. Rabani, *J. Phys. Chem.*, 1973, **77**, 2420–2424.

58 T. S. Rodrigues, M. Zhao, T.-H. Yang, K. D. Gilroy, A. G. M. da Silva, P. H. C. Camargo and Y. Xia, *Chem. Eur. J.*, 2018, **24**, 16944–16963.

59 M. Wang, A. Leff, Y. Li and T. Woehl, *ACS NANO*, 2021, **15**, 2578–2588.

60 L. E. Marbella, D. M. Chevrier, P. D. Tancini, O. Shobayo, A. M. Smith, K. A. Johnston, C. M. Andolina, P. Zhang, G. Mpourmpakis and J. E. Millstone, *J. Am. Chem. Soc.*, 2015, **137**, 15852–15858.

61 T. J. Woehl, C. Park, J. E. Evans, I. Arslan, W. D. Ristenpart and N. D. Browning, *Nano Lett.*, 2014, **14**, 373–378.

62 K. Gnanasekaran, K. M. Vailonis, D. M. Jenkins and N. C. Gianneschi, *ACS Nano*, 2020, **14**, 8735–8743.

63 K. Aliyah, J. Lyu, C. Goldmann, T. Bizien, C. Hamon, D. Alloyeau and D. Constantin, *J. Phys. Chem. Lett.*, 2020, **11**, 2830–2837.

64 S. F. Tan, G. Bisht, U. Anand, M. Bosman, X. E. Yong and U. Mirsaidov, *J. Am. Chem. Soc.*, 2018, **140**, 11680–11685.

65 Y. Xia, X. Xia and H.-C. Peng, *J. Am. Chem. Soc.*, 2015, **137**, 7947–7966.

66 T.-H. Yang, K. D. Gilroy and Y. Xia, *Chem. Sci.*, 2017, **8**, 6730–6749.

67 Q. N. Nguyen, R. Chen, Z. Lyu and Y. Xia, *Inorg. Chem.*, 2021, **60**, 4182–4197.

68 M. R. Hauwiller, J. C. Ondry, C. M. Chan, P. Khandekar, J. Yu and A. P. Alivisatos, *J. Am. Chem. Soc.*, 2019, **141**, 4428–4437.

69 X. Ye, M. R. Jones, L. B. Frechette, Q. Chen, A. S. Powers, P. Ercius, G. Dunn, G. M. Rotskoff, S. C. Nguyen, V. P. Adiga, A. Zettl, E. Rabani, P. L. Geissler and A. P. Alivisatos, *Science*, 2016, **354**, 874–877.

70 M. R. Hauwiller, L. B. Frechette, M. R. Jones, J. C. Ondry, G. M. Rotskoff, P. Geissler and A. P. Alivisatos, *Nano Lett.*, 2018, **18**, 5731–5737.

71 I. A. Moreno-Hernandez, M. F. Crook, J. C. Ondry and A. P. Alivisatos, *J. Am. Chem. Soc.*, 2021, **143**, 12082–12089.

72 M. F. Crook, I. A. Moreno-Hernandez, J. C. Ondry, J. Ciston, K. C. Bustillo, A. Vargas and A. P. Alivisatos, *J. Am. Chem. Soc.*, 2023, **145**, 6648–6657.

73 Y. Wang, D. Rastogi, K. Malek, J. Sun, A. Asa-Awuku and T. Woehl, *J. Phys. Chem. A*, 2023, **127**, 2545–2553.

74 M. Wang, C. Park and T. J. Woehl, *Chem. Mater.*, 2018, **30**, 7727–7736.

75 J. M. Grogan, N. M. Schneider, F. M. Ross and H. H. Bau, *Nano Lett.*, 2014, **14**, 359–364.

76 R. E. Robberstad Møller-Nilsen, S. Canepa, E. Jensen, H. Sun, I. A. Moreno-Hernandez, M. N. Yesibolati, A. P. Alivisatos and K. S. Mølhave, *J. Phys. Chem. C*, 2023, **127**, 15512-15522.

77 A. Heuer-Jungemann, N. Feliu, I. Bakaimi, M. Hamaly, A. Alkilany, I. Chakraborty, A. Masood, M. F. Casula, A. Kostopoulou, E. Oh, K. Susumu, M. H. Stewart, I. L. Medintz, E. Stratakis, W. J. Parak and A. G. Kanaras, *Chem. Rev.*, 2019, **119**, 4819–4880.

78 J. R. Reimers, M. J. Ford, A. Halder, J. Ulstrup and N. S. Hush, *Proc. Natl. Acad. Sci. U.S.A.*, 2016, **113**, E1424–E1433.

79 S. Mozaffari, W. Li, C. Thompson, S. Ivanov, S. Seifert, B. Lee, L. Kovarik and A. M. Karim, *Nanoscale*, 2017, **9**, 13772–13785.

80 W. Li, M. G. Taylor, D. Bayerl, S. Mozaffari, M. Dixit, S. Ivanov, S. Seifert, B. Lee, N. Shanaiah, Y. Lu, L. Kovarik, G. Mpourmpakis and A. M. Karim, *Nanoscale*, 2021, **13**, 206–217.

81 R. L. Clough, *Nucl. Instrum. Methods Phys. Res., Sect. B* , 2001, **185**, 8–33.

82 P. Ulanski and J. M. Rosiak, *Nucl. Instrum. Methods Phys. Res., Sect. B*, 1999, **151**, 356–360.

83 W. Gibson and J. P. Patterson, *Macromol.*, 2021, **54**, 4986–4996.

84 K. H. Nagamanasa, H. Wang and S. Granick, *Adv. Mater.*, 2017, **29**, 1703555.

85 A. Mirzahosseini and B. Noszál, *Sci. Rep.*, 2016, **6**, 37596.

86 J. Kang, Y.-X. Wang, F. Peng, N.-N. Zhang, Y. Xue, Y. Yang, E. Kumacheva and K. Liu, *Angew. Chem. Int. Ed.*, 2022, **61**, e202202405.

87 T. Gupta, N. M. Schneider, J. H. Park, D. Steingart and F. M. Ross, *Nanoscale*, 2018, **10**, 7702–7710.

88 J. Korpanty, L. R. Parent and N. C. Gianneschi, *Nano Lett.*, 2021, **21**, 1141–1149.

89 T. U. Dissanayake, M. Wang and T. J. Woehl, *ACS Appl. Mater. Interfaces*, 2021, **13**, 37553–37562.

90 P. Ulanski, E. Bothe, K. Hildenbrand, J. M. Rosiak and C. von Sonntag, *Radiat. Phys. Chem.*, 1995, **46**, 909–912.

91 P. Ulański, S. Kadłubowski and J. M. Rosiak, *Radiat. Phys. Chem.*, 2002, **63**, 533–537.

92 J. W. Yeh, *Annales De Chimie-Science Des Materiaux*, 2006, **31**, 633–648.

93 J.-W. Yeh, S.-K. Chen, S.-J. Lin, J.-Y. Gan, T.-S. Chin, T.-T. Shun, C.-H. Tsau and S.-Y. Chang, *Adv. Eng. Mater.*, 2004, **6**, 299–303.

94 S. Gao, S. Hao, Z. Huang, Y. Yuan, S. Han, L. Lei, X. Zhang, R. Shahbazian-Yassar and J. Lu, *Nat. Commun.*, 2020, **11**, 2016.

95 N. L. N. Broge, M. Bondesgaard, F. Søndergaard-Pedersen, M. Roelsgaard and B. B. Iversen, *Angew. Chem. Int. Ed.*, 2020, **59**, 21920–21924.

96 J. Zhang, H. Li, Q. Kuang and Z. Xie, *Acc. Chem. Res.*, 2018, **51**, 2880–2887.

97 D. Keller, T. R. Henninen and R. Erni, *Nanoscale*, 2020, **12**, 22511–22517.

98 W. Dachraoui, T. R. Henninen, D. Keller and R. Erni, *Sci. Rep.*, 2021, **11**, 23965.
99 T. R. Henninen, D. Keller and R. Erni, *Chemnanomat*, 2021, **7**, 110–116.
100 W. Dachraoui and R. Erni, *Chem. Mater.*, 2023, 35, 1201-1208.
101 A. H. Phakatkar, V. Yurkiv, P. Ghildiyal, Y. J. Wang, A. Amiri, L. V. Sorokina, M. R. Zachariah, T. Shokuhfar and R. Shahbazian-Yassar, *Acs Nano*, 2023, **17**, 5880–5893.
102 Z. Zheng, T. Tachikawa and T. Majima, *J. Am. Chem. Soc.*, 2014, **136**, 6870–6873.
103 C. J. Murphy, T. K. Sau, A. M. Gole, C. J. Orendorff, J. Gao, L. Gou, S. E. Hunyadi and T. Li, *J. Phys. Chem. B*, 2005, **109**, 13857–13870.
104 M.-W. Chu, V. Myroshnychenko, C. H. Chen, J.-P. Deng, C.-Y. Mou and F. J. García De Abajo, *Nano Lett.*, 2009, **9**, 399–404.
105 R. M. Sarhan, W. Koopman, R. Schuetz, T. Schmid, F. Liebig, J. Koetz and M. Bargheer, *Sci. Rep.*, 2019, **9**, 3060.
106 N. Ortiz, B. Zoellner, S. J. Hong, Y. Ji, T. Wang, Y. Liu, P. A. Maggard and G. Wang, *ACS Appl. Mater. Interfaces*, 2017, **9**, 25962–25969.
107 A. Movsesyan, E. Y. Santiago, S. Burger, M. A. Correa-Duarte, L. V. Besteiro, Z. Wang and A. O. Govorov, *Adv. Opt. Mater.*, 2022, **10**, 2102663.
108 G. V. Hartland, L. V. Besteiro, P. Johns and A. O. Govorov, *ACS Energy Lett.*, 2017, **2**, 1641–1653.
109 S. Hu, B.-J. Liu, J.-M. Feng, C. Zong, K.-Q. Lin, X. Wang, D.-Y. Wu and B. Ren, *J. Am. Chem. Soc.*, 2018, **140**, 13680–13686.
110 P. H. C. Camargo and E. Cortés, Eds., *Plasmonic catalysis: from fundamentals to applications*, Wiley-VCH, Weinheim, 2021.
111 Y. Yu, V. Sundaresan and K. A. Willets, *J. Phys. Chem. C*, 2018, **122**, 5040–5048.
112 E. S. Thrall, A. Preska Steinberg, X. Wu and L. E. Brus, *J. Phys. Chem. C*, 2013, **117**, 26238–26247.
113 Y. Dai, G. He, S. Long, X. Li, L. Meng, P. Wang, X. Li and Z. Yang, *ACS Appl. Nano Mater.*, 2023, **6**, 4946–4956.
114 A. S. Hainer, J. S. Hodgins, V. Sandre, M. Vallieres, A. E. Lanterna and J. C. Scaiano, *ACS Energy Lett.*, 2018, **3**, 542–545.
115 G. T. Forcherio, B. Ostovar, J. Boltersdorf, Y.-Y. Cai, A. C. Leff, K. N. Grew, C. A. Lundgren, S. Link and D. R. Baker, *ACS Nano*, 2022, **16**, 12377–12389.
116 G. T. Forcherio, D. R. Baker, J. Boltersdorf, A. C. Leff, J. P. McClure, K. N. Grew and C. A. Lundgren, *J. Phys. Chem. C*, 2018, **122**, 28901–28909.
117 G. T. Forcherio, D. R. Baker, A. C. Leff, J. Boltersdorf, J. P. McClure, K. N. Grew and C. A. Lundgren, *JoVE*, 2019, 60041.
118 A. L. Koh, K. Bao, I. Khan, W. E. Smith, G. Kothleitner, P. Nordlander, S. A. Maier and D. W. McComb, *ACS Nano*, 2009, **3**, 3015–3022.
119 J. Nelayah, M. Kociak, O. Stéphan, F. J. García De Abajo, M. Tencé, L. Henrard, D. Taverna, I. Pastoriza-Santos, L. M. Liz-Marzán and C. Colliex, *Nat. Phys*, 2007, **3**, 348–353.
120 P. Sutter, Y. Li, C. Argyropoulos and E. Sutter, *J. Am. Chem. Soc.*, 2017, **139**, 6771–6776.
121 M. Sun, Y. Li, B. Zhang, C. Argyropoulos, P. Sutter and E. Sutter, *Langmuir*, 2020, **36**, 2044–2051.
122 M. R. Langille, M. L. Personick and C. A. Mirkin, *Angew. Chem. Int. Ed.*, 2013, **52**, 13910–13940.
123 X. Chen, R. Wen, L. Zhang, A. Lahiri, P. Wang and Y. Fang, *Plasmonics*, 2014, **9**, 945–949.
124 R. Jin, Y. Cao, C. A. Mirkin, K. L. Kelly, G. C. Schatz and J. G. Zheng, *Science*, 2001, **294**, 1901–1903.
125 R. Jin, Y. Charles Cao, E. Hao, G. S. Métraux, G. C. Schatz and C. A. Mirkin, *Nature*, 2003, **425**, 487–490.
126 A. Chen, A. C. Leff, G. T. Forcherio, J. Boltersdorf and T. J. Woehl, *J. Phys. Chem. Lett.*, 2023, **14**, 1379–1388.
127 G. Porter, Ed., *Progress in reaction Kinetics. Volume 3*, Pergamon Press, Oxford, 1965.

128 A. W. Mureithi, Y. Sun, T. Mani, A. R. Howell and J. Zhao, *Cell Rep. Phys. Sci.*, 2022, **3**, 100889.
129 T. Tan, D. Beydoun and R. Amal, *J. Photochem. Photobiol. A*, 2003, **159**, 273–280.
130 L. Qiao, N. Pollard, R. D. Senanayake, Z. Yang, M. Kim, A. S. Ali, M. T. Hoang, N. Yao, Y. Han, R. Hernandez, A. Z. Clayborne and M. R. Jones, *Nat. Commun.*, 2023, **14**, 4408.
131 M. N. Yesibolati, S. Laganà, H. Sun, M. Beleggia, S. M. Kathmann, T. Kasama and K. Mølhave, *Phys. Rev. Lett.*, 2020, **124**, 065502.
132 J. T. van Omme, H. Wu, H. Sun, A. F. Beker, M. Lemang, R. G. Spruit, S. P. Maddala, A. Rakowski, H. Friedrich, J. P. Patterson and H. H. Pérez Garza, *J. Mater. Chem. C*, 2020, **8**, 10781–10790.
133 P. Abellan, B. L. Mehdi, L. R. Parent, M. Gu, C. Park, W. Xu, Y. Zhang, I. Arslan, J.-G. Zhang, C.-M. Wang, J. E. Evans and N. D. Browning, *Nano Lett.*, 2014, **14**, 1293–1299.
134 P. Abellan, L. R. Parent, N. Al Hasan, C. Park, I. Arslan, A. M. Karim, J. E. Evans and N. D. Browning, *Langmuir*, 2016, **32**, 1468–1477.
135 N. Bhattarai, D. L. Woodall, J. E. Boercker, J. G. Tischler and T. H. Brintlinger, *Nanoscale*, 2019, **11**, 14573–14580.
136 J. Weiss and C. H. Collins, *Rad. Res.*, 1966, **28**, 1–12.
137 L. H. Gale, B. E. Gordon, G. Steinberg and C. D. Wagner, *J. Phys. Chem.*, 1962, **66**, 1538–1539.
138 R. B. Ingalls, *J. Phys. Chem.*, 1961, **65**, 1605–1608.
139 J. Wu, W. Gao, J. Wen, D. J. Miller, P. Lu, J.-M. Zuo and H. Yang, *Nano Lett.*, 2015, **15**, 2711–2715.
140 Y. Sun and Y. Xia, *Science*, 2002, **298**, 2176–2179.
141 X. Peng, L. Manna, W. Yang, J. Wickham, E. Scher, A. Kadavanich and A. P. Alivisatos, *Nature*, 2000, **404**, 59–61.
142 S. Lee, N. M. Schneider, S. F. Tan and F. M. Ross, *ACS Nano*, 2023, **17**, 5609–5619.
143 A. Khelfa, J. Nelayah, H. Amara, G. Wang, C. Ricolleau and D. Alloyeau, *Adv. Mater.*, 2021, **33**, 2102514.
144 K. Karki, P. Kumar, A. Verret, N. Glachman, D. H. Alsem, D. Jariwala, N. Salmon and E. Stach, *Microsc. Microanal.*, 2020, **26**, 2446–2447.
145 J. E. Evans, K. L. Jungjohann, N. D. Browning and I. Arslan, *Nano Lett.*, 2011, **11**, 2809–2813.
146 X. Fu, B. Chen, J. Tang and A. H. Zewail, *Sci. Adv.*, 2017, **3**, e1701160.
147 U. J. Lorenz and A. H. Zewail, *Science*, 2014, **344**, 1496–1500.
148 JEOL-IDES Products | Products | JEOL Ltd., https://www.jeol.com/products/scientific/tem/JEOL-IDES_Products.php, (accessed June 3, 2023).
149 H. Liu, T. E. Gage, P. Singh, A. Jaiswal, R. D. Schaller, J. Tang, S. T. Park, S. K. Gray and I. Arslan, *Nano Lett.*, 2021, **21**, 5842–5849.